New Journal of Physics
The open access journal at the forefront of physics

Deutsche Physikalische Gesellschaft DPG
IOP Institute of Physics

Published in partnership with: Deutsche Physikalische Gesellschaft and the Institute of Physics

OPEN ACCESS

RECEIVED
20 August 2018

REVISED
4 December 2018

ACCEPTED FOR PUBLICATION
12 December 2018

PUBLISHED
5 February 2019

PAPER

On the existence of superradiant excitonic states in microtubules

G L Celardo[1], M Angeli[2,3], T J A Craddock[4,5,9] and P Kurian[6,7,8,9]

[1] Benemérita Universidad Autónoma de Puebla, Apartado Postal J-48, Instituto de Física, 72570, Mexico
[2] International School for Advanced Studies (SISSA), Via Bonomea 265, I-34136 Trieste, Italy
[3] Dipartimento di Matematica e Fisica and Interdisciplinary Laboratories for Advanced Materials Physics, Università Cattolica del Sacro Cuore, via Musei 41, I-25121 Brescia, Italy
[4] Departments of Psychology and Neuroscience, Computer Science, and Clinical Immunology, Nova Southeastern University, Fort Lauderdale FL 33314, United States of America
[5] Clinical Systems Biology Group, Institute for Neuro-Immune Medicine, Fort Lauderdale FL 33314, United States of America
[6] Quantum Biology Laboratory, Howard University, Washington DC 20059, United States of America
[7] Center for Computational Biology and Bioinformatics, Howard University College of Medicine, Washington DC 20059, United States of America
[8] Department of Physics and Astronomy, University of Iowa, Iowa City IA 52242, United States of America
[9] Authors to whom any correspondence should be addressed.

E-mail: celardo@ifuap.buap.mx, mangeli@sissa.it, tcraddock@nova.edu and pkurian@howard.edu

Keywords: quantum biology, quantum transport in disordered systems, open quantum systems, energy transfer

Abstract

Microtubules are biological protein polymers with critical and diverse functions. Their structures share some similarities with photosynthetic antenna complexes, particularly in the ordered arrangement of photoactive molecules with large transition dipole moments. As the role of photoexcitations in microtubules remains an open question, here we analyze tryptophan molecules, the amino acid building block of microtubules with the largest transition dipole strength. By taking their positions and dipole orientations from realistic models capable of reproducing tubulin experimental spectra, and using a Hamiltonian widely employed in quantum optics to describe light–matter interactions, we show that such molecules arranged in their native microtubule configuration exhibit a superradiant lowest exciton state, which represents an excitation fully extended on the chromophore lattice. We also show that such a superradiant state emerges due to supertransfer coupling between the lowest exciton states of smaller blocks of the microtubule. In the dynamics we find that the spreading of excitation is ballistic in the absence of external sources of disorder and strongly dependent on initial conditions. The velocity of photoexcitation spreading is shown to be enhanced by the supertransfer effect with respect to the velocity one would expect from the strength of the nearest-neighbor coupling between tryptophan molecules in the microtubule. Finally, such structures are shown to have an enhanced robustness to static disorder when compared to geometries that include only short-range interactions. These cooperative effects (superradiance and supertransfer) may induce ultra-efficient photoexcitation absorption and could enhance excitonic energy transfer in microtubules over long distances under physiological conditions.

1. Introduction

From the suggestion [1, 2] that coherent wave behavior might be implicated in excitonic transport for natural photosynthetic systems under ambient conditions, ample motivation has since arisen to investigate the relevance of quantum mechanical behavior in diverse biological networks of photoactive molecules. For instance, in photosynthetic systems, great attention has been devoted to the antenna complexes. Such complexes are made of a network of chlorophyll molecules (photoactive in the visible range), which are able to absorb sunlight and transport the excitation to a specific molecular aggregate (the reaction center). The reaction center is where charge separation occurs, in order to trigger the ensuing steps required for carbon fixation [3].

Some of the dominant coherent effects which are thought to be responsible for the high efficiency of natural photosynthetic complexes are induced by the delocalization of the excitation over many molecules[10]. Such delocalized excitonic states can lead to cooperative effects, such as superabsorption and supertransfer [3, 4], and they can be useful in both natural and engineered light-harvesting complexes [5–20]. Specifically, delocalized excitonic states can have a much larger dipole strength than that of the constituent chromophores, and such giant transient dipoles [21–23] can strongly couple to the electromagnetic field. Thus, these states are able to superabsorb light, i.e. they are able to absorb light at a rate which is much larger than the single-molecule absorbing rate [23]. Indeed, the absorption rate of delocalized excitonic states can increase with the number of molecules over which the excitation is delocalized [22, 23]. Supertransfer is described in a similar way, with respect to movement of the excitation to an external molecular aggregate or between different parts of the same system [4]. Specifically, an excitonic state delocalized on N molecules of one molecular aggregate can couple with an excitonic state delocalized on M molecules of a second aggregate with a coupling amplitude which is $\sqrt{NM}$ times larger than the coupling amplitude between single molecules belonging to different aggregates. Such supertransfer coupling is able to enhance the velocity of spreading of photoexcitations, and it has been shown to have an important role in natural photosynthetic systems [24].

The role of coherent energy transfer has been investigated not only in photosynthetic complexes but also in other important biomolecular polymers, such as in cytoskeletal microtubules [25, 26] and in DNA [27]. In this paper we will focus on the role of photoexcitations in microtubules, which are essential biomolecular structures that have multiple roles in the functionality of cells. Indeed, microtubules are present in every eukaryotic cell to provide structural integrity to the cytoskeletal matrix, and they are thought to be involved in many other cellular functions, including motor trafficking, cellular transport, mitotic division, and cellular signaling in neurons. Interestingly, microtubules share some structural similarities with photosynthetic antenna complexes, such as the cylindrical arrangement of chlorophyll molecules in phycobilisome antennas [28] or in green sulphur bacteria [29], where cylinders made of more than 10^5 chlorophyll molecules can efficiently harvest sunlight for energy storage in the form of sugar. Note that while chlorophyll molecules are active in the visible range of electromagnetic radiation, microtubules possess an architecture of chromophoric molecules (i.e. aromatic amino acids like tryptophan) which are photoactive in the ultraviolet (UV) range.

It remains an open question whether microtubules have any role in transporting cellular photoexcitations. Intriguingly, several groups have studied and experimentally confirmed the presence of very weak endogenous photon emissions within the cell across the UV, visible, and IR spectra [30–34]. It has also been suggested that microtubules may play a role in cellular orientation and 'vision' via the centrosome complex [35], and very recently two of us have proposed neuronal signaling pathways in microtubules via coherent excitonic transport [26].

Each mammalian microtubule is composed of 13 protofilaments, which form a helical-cylindrical arrangement of tubulin subunit protein dimers, as in figure 1. The tubulin subunit proteins possess a unique network of chromophores, namely different amino acids, which can form excited state transition dipoles in the presence of photons. The geometry and dipole moments of these amino acids, which are termed *aromatic* owing to their largely delocalized π electrons, are similar to those of photosynthetic constituents, indicating that tubulin may support coherent energy transfer. As with chlorophyll molecules, it is possible to associate to each aromatic amino acid a transition dipole that determines its coupling to other molecules and with the electromagnetic field.

The main question we address in this paper is whether the arrangement of photoactive molecules in the microtubule structure can support extended excitonic states with a giant dipole strength, at least in the absence of environmental disorder. Such extended states, if robust to noise, can also support efficient transport of photoexcitations, which could have a biological role in microtubule signaling between cells and across the brain [26]. To answer this question, we consider first a quantum description of the network of tryptophan molecules, which are the greatest contributor to photoabsorption in microtubules in the UV range. Indeed, tryptophan is the aromatic amino acid with the largest transition dipole (6.0 debye), comparable with that of chlorophyll molecules. We proceed by modeling these tryptophans as two-level systems, as is usually done in photosynthetic antenna complexes. This is, to our knowledge, the first analysis of excitonic states distributed across tryptophan chromophore lattices in large-scale, realistic models of microtubules.

The interaction between the transition dipoles of the photoactive molecules is in general very complicated, with the common coupling to the electromagnetic field more nuanced than simple dipole–dipole interactions, which are an effective description of a chromophoric network only in the small-size limit (where the system size

[10] There is substantial debate among experimentalists regarding the role of delocalization in excitonic transport. In part this is due to a multiplicity of definitions for 'coherence.' In this paper we will not discuss coherence in the context of oscillatory beating patterns observed in the exciton state over multiple chromophores [1, 2]. Instead, we are interested in the collective response of a network of chromophores, excited by light whose wavelength is of the same order as the network size.

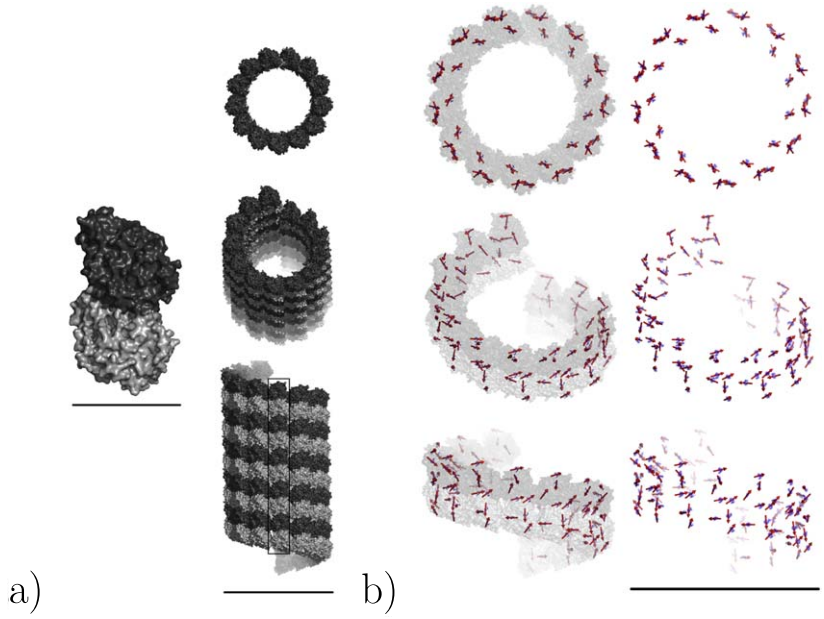

Figure 1. Panel (a): tubulin dimer and microtubule segment. Left: solvent-excluded tubulin heterodimer surface with α-tubulin monomer in light grey, and β-tubulin monomer in dark grey (scale bar ∼5 nm). Right: section of microtubule B-lattice structure at three angles showing left-handed helical symmetry and protofilament (bottom, outlined in black box) (scale bar ∼25 nm). In microtubules, tubulin dimers stack end-to-end to form the protofilaments, 13 of which join side-by-side with longitudinal offset and wrap around to form a tube with such helical symmetry. Panel (b): arrangement of tryptophan amino acids in microtubule segment at three angles with transition dipole directions. Left: a single spiral of tubulin dimers (light grey α-tubulin, dark grey β-tubulin) from microtubule structure showing tryptophan amino acids (blue sticks) and transition dipole directions (red arrows). Right: tryptophan amino acids and transition dipole directions only (scale bar ∼25 nm).

is much smaller then the wavelength) [36]. However, for large aggregates one needs to go beyond the simple dipole–dipole interactions used in small aggregates. Here we consider an effective non-Hermitian Hamiltonian interaction commonly used in the literature to study the coupling in molecular aggregates [22]. This non-Hermitian description also allows the possibilities of donating the excitation back to the electromagnetic field through photon emission or of transferring excitation coherently between chromophores. Moreover, in the small-system-size limit it reduces to a dipole–dipole interaction.

The imaginary part of the complex eigenvalues $\mathcal{E} = E - \mathrm{i}\Gamma/2$ of such a non-Hermitian Hamiltonian determines the strength of the coupling of the excitonic states with the electromagnetic field and is connected with the dipole strength of the eigenstates of the system. While the coupling of a single aromatic molecule can be characterized by its decay rate γ, Γ determines the coupling of extended excitonic states with the electromagnetic field. Superradiant states are characterized by $\Gamma > \gamma$, while subradiant states are characterized by $\Gamma < \gamma$. Most importantly, for superradiant states, Γ should be proportional to the number of chromophores N, for $L \leqslant \lambda$, where L is the system length and λ is the wavelength of the aromatic molecule optical transition, and begins to saturate for $L > \lambda$. Note that $\hbar/\Gamma$ is the lifetime of the excitonic eigenstate, so that larger values of Γ govern faster excitation decays. Since the process is symmetric under time reversal, fast decaying states are also fast absorbing states. The advantage of this formalism, with respect to the simple dipole–dipole interaction commonly used in the literature, is that it allows us to consider system sizes that are even larger than the wavelength of the absorbed light. This property becomes particularly important for large biopolymeric structures like microtubules whose length is generally several orders of magnitude larger than the wavelength associated with the molecular transitions ($\lambda = 280$ nm). Here we consider microtube lengths up to $\sim 3\lambda$.

We use data on the positions, dipole orientations, and excitation energies of tryptophan molecules, which have been obtained by molecular dynamics simulations and quantum chemistry calculations [25, 26]. These data have been shown to reproduce well the absorption, circular dichroism, and linear dichroism spectra of single tubulin dimers [25, 26].

Our analysis shows that as the number of tubulin subunits considered grows, a superradiant state forms in the lowest exciton state of the system. This is exactly what happens in many photosynthetic antenna complexes, such as in green sulfur bacteria cylindrical antennas [19, 20, 37] and in self-assembled molecular nanotubes [38–43]. Superradiant states favor the absorption of photons by the microtubule. Moreover, since the superradiant lowest exciton state represents an extended (delocalized) excitonic state of the order of the microtubule length, such superradiant states could serve as a support for efficient transport of photoexcitation.

In the next section we develop the mathematical machinery for our physical model, using an effective Hamiltonian that has been widely used to describe a single photoexcitation interacting within a network of transient dipoles. In section 3 we display several results demonstrating the existence of a superradiant excitonic state extended over more than 10^4 tryptophan molecules of the microtubule. We also show that the superradiant lowest exciton state emerges from the supertransfer coupling between the lowest exciton states of smaller segments inside the microtubule. Section 4 shows initial studies of the exciton dynamics, showing that cooperativity can enhance the coupling between different parts of the microtubule through supertransfer. Section 5 demonstrates the robustness of the superradiant lowest exciton state to disorder, and we close in section 6 with some conclusions and our future outlook.

2. The model

Microtubules are cylindrical-helical structures made of essentially two closely related proteins, α- and β-tubulin. They are arranged as in figure 1 to form a left-handed helical tube of protofilament strands. In each α–β dimer there are many aromatic molecules: eight tryptophans (Trps) whose transition dipoles are arranged as in figure 1 (see appendix A for complete description). Their peak excitation energy is ∼280 nm, and the magnitude of their dipole moment is 6.0 debye. There also exist other aromatics, including tyrosine, phenylalanine, and histidine, with much smaller dipole moments. For example, tyrosine (the molecule with the second largest dipole) has a dipole moment of only 1.2 debye. For the purposes of this initial analysis, we limit our attention to the Trps only because of their relatively large transition dipoles. The position and orientation of the dipole moments of Trp molecules have been obtained from molecular dynamics and quantum chemistry calculations, and they reproduce closely the linear and circular dichroism spectra of tubulin for the Trp-only case [25, 26].

The interaction of a network of dipoles with the electromagnetic field is well described by the effective Hamiltonian [22, 44, 45]

$$H_{\rm eff} = H_0 + \Delta - \frac{\rm i}{2}G, \tag{1}$$

where H_0 represents the sum of the excitation energies of each molecule, and Δ and G represent the coupling matrices (elements listed below in equations (3)–(5)) between the molecules induced by the interaction with the electromagnetic field. Note that such an effective Hamiltonian has been widely used to model light–matter interactions in the approximation of a single excitation. The site energies are all identical, so that we have

$$\begin{aligned} H_0 &= \sum_{n=1}^{N} \hbar\omega_0 |n\rangle\langle n|, \quad \Delta = \sum_{n}^{N} \Delta_{nn}|n\rangle\langle n| + \sum_{n\neq m}^{N} \Delta_{nm}|n\rangle\langle m|, \\ G &= \sum_{n}^{N} G_{nn}|n\rangle\langle n| + \sum_{n\neq m}^{N} G_{nm}|n\rangle\langle m|. \end{aligned} \tag{2}$$

The wavenumber associated with each site energy is $k_0 := \omega_0 n_r/c$, where c is the speed of light and $n_r = \sqrt{\mu_r \epsilon_r}$ is the refractive index. Most natural materials are non-magnetic at optical frequencies (relative permeability $\mu_r \approx 1$) so we can assume that $n_r \sim \sqrt{\epsilon_r}$. The real and imaginary parts of the intermolecular coupling are given on the diagonal, respectively, by

$$\Delta_{nn} = 0, \qquad G_{nn} = \frac{4}{3}\frac{\mu^2}{\epsilon_r}k_0^3 =: \gamma, \tag{3}$$

with $\mu = |\vec{\mu}|$ being the magnitude of the transition dipole of a single tryptophan and ϵ_r being the relative permittivity, and on the off-diagonal, respectively, by [9, 22, 44]

$$\begin{aligned} \Delta_{nm} = \frac{3\gamma}{4}\Bigg[&\left(-\frac{\cos(k_0 r_{nm})}{(k_0 r_{nm})} + \frac{\sin(k_0 r_{nm})}{(k_0 r_{nm})^2} + \frac{\cos(k_0 r_{nm})}{(k_0 r_{nm})^3}\right)\hat{\mu}_n \cdot \hat{\mu}_m \\ &- \left(-\frac{\cos(k_0 r_{nm})}{(k_0 r_{nm})} + 3\frac{\sin(k_0 r_{nm})}{(k_0 r_{nm})^2} + 3\frac{\cos(k_0 r_{nm})}{(k_0 r_{nm})^3}\right)(\hat{\mu}_n \cdot \hat{r}_{nm})(\hat{\mu}_m \cdot \hat{r}_{nm})\Bigg], \end{aligned} \tag{4}$$

$$\begin{aligned} G_{nm} = \frac{3\gamma}{2}\Bigg[&\left(\frac{\sin(k_0 r_{nm})}{(k_0 r_{nm})} + \frac{\cos(k_0 r_{nm})}{(k_0 r_{nm})^2} - \frac{\sin(k_0 r_{nm})}{(k_0 r_{nm})^3}\right)\hat{\mu}_n \cdot \hat{\mu}_m \\ &- \left(\frac{\sin(k_0 r_{nm})}{(k_0 r_{nm})} + 3\frac{\cos(k_0 r_{nm})}{(k_0 r_{nm})^2} - 3\frac{\sin(k_0 r_{nm})}{(k_0 r_{nm})^3}\right)(\hat{\mu}_n \cdot \hat{r}_{nm})(\hat{\mu}_m \cdot \hat{r}_{nm})\Bigg], \end{aligned} \tag{5}$$

where $\hat{\mu}_n := \vec{\mu}_n/\mu$ is the unit dipole moment of the nth site and $\hat{r}_{nm} := \vec{r}_{nm}/r_{nm}$ is the unit vector joining the nth and the mth sites. In the following we assume $\epsilon_r = 1 = n_r$, corresponding to their values in vacuum/air.

The actual dielectric constant and refractive index of tubulin is currently debated [26, 34], but using the tubulin dielectric instead of air would increase the imaginary part of the coupling by $\sqrt{2} \leqslant \sqrt{\epsilon_r} \leqslant \sqrt{8.41}$, depending on the value chosen, which would proportionally decrease the lifetimes of the excitonic eigenstates. The real part of the off-diagonal coupling would also be increased by the same factor, augmenting the dipole strength of the excitonic state.

The eigenvalues of this Hamiltonian are complex, endowing the eigenstates with a finite lifetime due to their coupling to the external environment. The imaginary part of an eigenvalue is directly linked to the decay rate Γ of the eigenstate. Thus for each eigenmode of the system, Γ represents its coupling to the electromagnetic field. For $\Gamma > \gamma$ we have excitonic states which are coupled to the field more strongly than the single constituent molecule, representing superradiant states. On the other hand, the states for which $\Gamma < \gamma$ are subradiant. Since the sum of all the widths of the excitonic states of a system must be equal to $N\gamma$, where N is the total number of chromophores, superradiant states are always found in conjunction with subradiant states. Note that in a large ensemble of molecules, a certain degree of symmetry is needed to manifest superradiant and subradiant states [36]. In fact, a disordered network of dipoles suppresses superradiance, as we show below.

The non-Hermitian character of the Hamiltonian in equation (1) is due to the fact that the ensemble of photoactive molecules is not a closed system, since it interacts with the continuum of the electromagnetic field where the excitation can be radiatively lost. The analysis of open quantum systems within the framework of non-Hermitian Hamitonians is well-developed [5, 6, 46, 47] and used in the field of quantum optics with applications to photosynthetic complexes [22]. In this framework, the eigenstates of the non-Hermitian Hamiltonian represent the projection on the single excitation manifold of the true eigenstates of the molecular aggregate including also the photon degrees of freedom. So, if we indicate as $|\mathcal{E}\rangle$ the eigenstate of the non-Hermitian Hamiltonian,

$$P(k) = \frac{|\langle k|\mathcal{E}\rangle|^2}{\sum_k |\langle k|\mathcal{E}\rangle|^2} \tag{6}$$

represents the conditional probability to find the excitation on site k given that the excitation is in the system and not in the photon field. The time evolution of an initial state $|\psi_0\rangle$ can be computed as

$$|\psi(t)\rangle = \mathrm{e}^{-\mathrm{i}H_{\mathrm{eff}}t/\hbar}|\psi_0\rangle,$$

and $|\psi(t)\rangle$ represents the projection on the single excitation manifold of the molecular aggregate full wavefunction (including also the photon field degrees of freedom) at time t. In order to compute such time evolution one has to consider that right $|\mathcal{E}^R\rangle$ and left $|\mathcal{E}^L\rangle$ eigenstates for a symmetric non-Hermitian Hamiltonian are the transpose of each other and not the Hermitian conjugate of each other. Moreover they represent a complete bi-orthogonal basis set: $\langle\mathcal{E}^L_l|\mathcal{E}^R_m\rangle = \delta_{lm}$, which implies that the right eigenvectors are normalized such that $\sum_k(\langle k|\mathcal{E}^R\rangle)^2 = 1$. Given an initial state $|\psi_0\rangle$, its decomposition reads: $|\psi_0\rangle = \sum_k \langle\mathcal{E}^L_k|\psi_0\rangle\,|\mathcal{E}^R_k\rangle$. Note that from such a decomposition we can easily compute the time evolution of any initial state. We will make use of the above considerations in the following sections.

The parameters considered in our analysis are [25, 26]:

- $e_0 = 280$ nm $= 35\,716.65$ cm^{-1} as the Trp excitation energy,
- $k_0 = 2\pi e_0 \times 10^{-8} = 2.24 \times 10^{-3}$ Å^{-1} as the angular wavenumber,
- $\mu = 6\,D$ as the strength of the transition dipole between the ground state and the first excited state, with $\mu^2 \approx 181\,224$ Å^3 cm^{-1} (see the conversion[11]),
- $\gamma = 4\mu^2 k_0^3/3 = 2.73 \times 10^{-3}$ cm^{-1}, where $\gamma/\hbar$ is the radiative decay rate of a single Trp molecule, corresponding to the radiative lifetime $\tau_\gamma \approx 1.9$ ns (see the conversion[12]), and
- $n_s = 104$ as the number of dipoles per microtubule spiral.

[11] Let us recall that the units of the dipole–dipole interaction energy are given by $[E] = [\mu]^2[d]^{-3}$, where $[\mu]$ is the dipole unit and $[d]$ the distance unit. We express the dipoles in D (Debye), the distance in Å, and the energy in cm^{-1} units (applying the standard conversion $E/(hc)$, with h being the Planck constant and c the speed of light), so that $[\mu^2/(hc)] = \mathrm{cm}^{-1}\,\text{Å}^3$. Now, from the definition $1\mathrm{D} = 10^{-18}\,\mathrm{cm}^{5/2}\,\mathrm{g}^{1/2}\,\mathrm{s}^{-1}$ we have $1\mathrm{D}^2 = 10^{-12}\,\mathrm{cm}^2\,\mathrm{g}\,\mathrm{s}^{-2}\,\text{Å}^3$. Recalling the Planck constant $h = 6.626 \times 10^{-27}\,\mathrm{cm}^2\,\mathrm{g}\,\mathrm{s}^{-1}$ and the speed of light $c = 2.998 \times 10^{10}$ cm s^{-1}, we have $1\ \mathrm{D}^2/(hc) = 5034\ \mathrm{cm}^{-1}\,\text{Å}^3$. So, a transition dipole $\mu = \sqrt{36}$ D results in $\mu^2 = 36 \times 5034\ \mathrm{cm}^{-1}\,\text{Å}^3 = 181\,224\ \mathrm{cm}^{-1}\,\text{Å}^3$. Note that in these calculations we write explicitly where the energy is divided by hc for clarity, while in the main text we always assume implicitly that any energy is divided by hc.

[12] The lifetime related to an energy decay width γ is defined as $\tau_\gamma = \hbar/\gamma$. Note that we implicitly divide each energy or coupling by hc (with h and c defined in footnote 11), so that $[\gamma/(hc)] = \mathrm{cm}^{-1}$. Therefore, the units of the lifetime are given by $[\tau_\gamma] = \frac{1}{2\pi}\left[\frac{\hbar}{\gamma}\right] = (2\pi[c] \times \mathrm{cm}^{-1})^{-1}$, where $c = 2.998 \times 10^{-2}$ cm ps^{-1}. Thus, given a width in cm^{-1} units, its lifetime is obtained by multiplying the width by $2\pi c = 0.1884$ cm ps^{-1} and taking the reciprocal of the result.

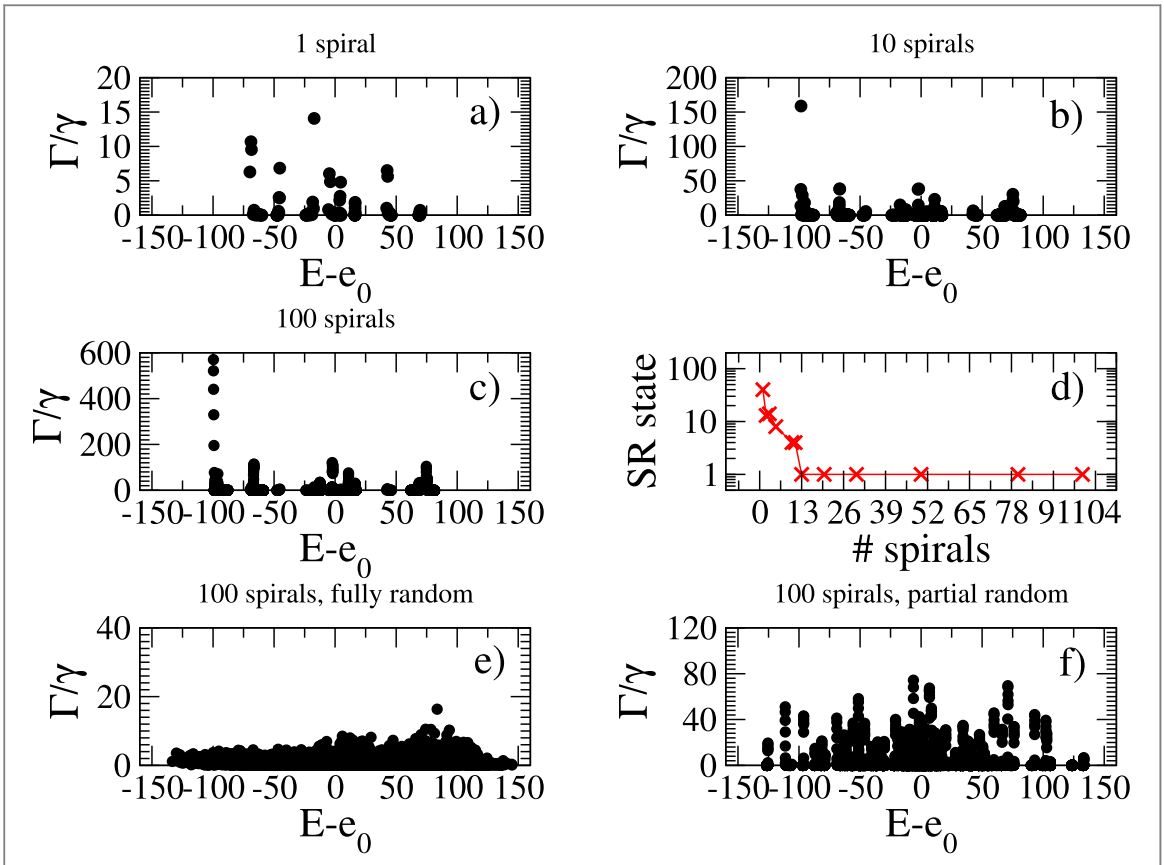

Figure 2. Panels (a)–(f): Normalized decay widths Γ/γ of the excitonic eigenstates are plotted versus their energies for microtubule segments of different lengths (number of spirals). Note that each spiral contains 104 tryptophan molecules and extends about 9 nm in the longitudinal direction. In panel (c) the maximum length of the microtubule segments considered in this paper is shown, comprised of 100 spirals and 10 400 tryptophan molecules. In panel (e) a microtubule of the same length (100 spirals) is shown; the positions of the tryptophans are the same as in panel (c), but the orientations of their dipoles are randomized. In panel (f) a microtubule of 100 spirals is shown; the positions of the tryptophans are the same as in panel (c), but the orientations of their dipoles are randomized in only one spiral and then repeated in all the other spirals. Finally in panel (d) the location in the energy spectrum of the superradiant state is shown as a function of the number of spirals. The superradiant state coincides with the lowest exciton state (state 1) for all microtubule segments of length greater than 12 spirals.

It should be noted that for small systems ($k_0 r_{nm} \ll 1$) the coupling terms in the Hamiltonian (1) become

$$G_{nm} \simeq \gamma \hat{\mu}_n \cdot \hat{\mu}_m,$$
$$\Delta_{nm} \simeq \frac{\vec{\mu}_n \cdot \vec{\mu}_m - 3(\vec{\mu}_n \cdot \hat{r}_{nm})(\vec{\mu}_m \cdot \hat{r}_{nm})}{r_{nm}^3}. \quad (7)$$

Here we have neglected terms that go as $1/r_{nm}$ because they are dominated by $1/r_{nm}^3$ contributions. In this limit, the real part Δ_{nm} represents a dipole–dipole interaction energy with $\mu = |\vec{\mu}_n| = |\vec{\mu}_m|$ and the radiative decay width $\gamma = \frac{4}{3}\mu^2 k_0^3$. Recall that this familiar dipole–dipole coupling which is used to describe the interactions between the transition dipoles of photoactive molecules cannot be used in our case, since this approximation is valid only when the size of the system L is much smaller then the wavelength λ associated with the transient dipole. In our analysis we consider microtubule lengths which are larger than λ. Thus in our case it is mandatory to go beyond the dipole–dipole approximation (see discussion in appendix B).

3. Superradiance in the lowest exciton state

We have diagonalized the full radiative Hamiltonian given in equation (1) for microtubule segments of different sizes, up to a microtubule more than 800 nm long and comprised of 100 spirals, including a total of 10 400 Trp molecules, so that $L/\lambda \approx 3$. For each eigenstate and complex eigenvalue $\mathcal{E} = E - i\Gamma/2$, we plot the decay width Γ of each state normalized to the single dipole decay width $\gamma = 2.73 \times 10^{-3}$ cm^{-1}.

In figure 2 we show how cooperativity (superradiance) emerges as we increase the number of spirals in the microtubule segment (where each spiral contains 104 Trp molecules). For one spiral (figure 2), there is a very disordered distribution of the decay widths, but as we increase the number of spirals a superradiant lowest exciton state clearly emerges with a decay width $\Gamma > \gamma$ that increases as we increase the length of the

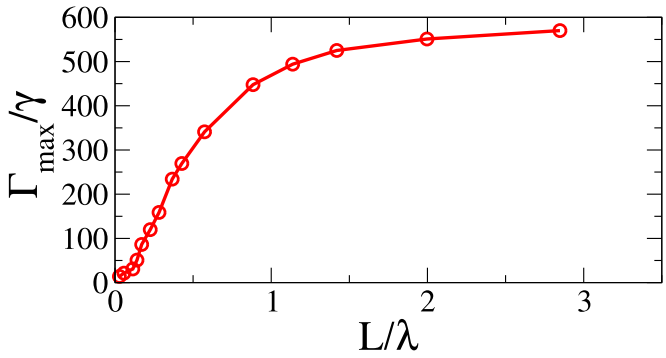

Figure 3. The maximum normalized decay width of the microtubule Γ_{max}/γ is shown as a function of the microtubule length L rescaled by the wavelength of the light that excites the atoms, $\lambda = 280$ nm.

microtubule segment. In figure 2 the normalized decay widths Γ/γ versus energies of the eigenstates of the microtubule comprised of 100 spirals are shown. As one can see, most of the decay width is concentrated in the lowest exciton state. The lowest-energy superradiant state in figure 2 corresponds to ∼600 times the single-molecule decay rate. In figure 2 the location in the energy spectrum of the largest superradiant state is shown as a function of the number of spirals. The energy of the largest superradiant state is indicated by an integer, where one means that the superradiant state is in the lowest exciton state, two that it is in the next excited state, etc. As one can see for all microtubule segments with number of spirals greater than 12, the superradiant state is in the lowest exciton state. The large decay width of the superradiant lowest exciton state indicates that such structures could be able to absorb photons ultra-efficiently. Indeed, the decay width of the lowest exciton state of the microtubule is in this case almost 600 times larger than the single-molecule decay width, corresponding to a value of roughly 1.64 cm^{-1}. This translates to an absorbing time scale of $\hbar/\Gamma \approx 3.2$ ps, which is very fast and comparable with the typical thermal relaxation times for biological structures [48], suggesting that non-equilibrium processes might be relevant in this regime.

The superradiant state (that with the highest decay width) exists for all microtubule segments, but the superradiant state coincides with the lowest exciton state only for segments of 13 or more spirals. An intuitive approach would suggest that, for 13 spirals, the microtubule topology becomes a 'square' manifold: 13 protofilaments $\times$ 13 spirals, such that if the cylinder were cut along its seam, one would obtain a sheet of tubulins 13 $\times$ 13 square. At this point the length of the cylinder (∼100 nm) begins to far outstrip its circumference (∼75 nm), and it is around this length that supertransfer processes (see section 3.1, below) become important, leading to the formation of a superradiant lowest exciton state.

The existence of a superradiant lowest exciton state is surprising considering that the positions and orientations of the dipoles may look quite disordered at first sight, as shown in figure 1(b). It is well known that interactions between molecules can destroy superradiance [36] unless dipole orientations have a certain degree of symmetry. The orientations of the Trp dipoles in the microtubule are far from being random, and their symmetry plays an important role. To show this we consider two additional models where the positions of the dipoles are the same as in the realistic case but with their orientations randomized. First we consider the case where the orientations of the dipoles are fully randomized over the whole microtubule length. In such a case the superradiance is completely suppressed, as shown in figure 2. Note also that in figure 2 the decay widths are distributed over many states, in contrast to the case of the native orientations of the dipoles, where most of the decay width of the system is concentrated in the lowest exciton state. The maximum value of the decay width for randomized dipoles in 100 spirals is much smaller than that of the superradiant lowest exciton state shown in figure 2, and even smaller than some decay widths shown in figure 2 for one spiral. One might also think that the emergence of a superradiant lowest exciton state is connected with the fact that the same dipole geometry is repeated over all the spirals. To show that this is not the case, we considered a second random model with random orientations of dipoles on a single spiral repeated over all other spirals. For this partial random model we still do not achieve a superradiant lowest exciton state, as shown in figure 2.

In order to understand how the superradiant decay width increases with the system size, in figure 3 the maximum decay width is plotted as a function of the length of the microtubule segment. Note that the decay width increases with the system size, but saturation occurs when the length of the microtubule is larger than λ, the wavelength associated with absorption by the transient dipoles.

Such a large decay width of the superradiant lowest exciton state indicates that the excitation in the lowest-energy state is extended over many Trp molecules. In the upper panels of figure 4, the probability of finding the excitation on each Trp molecule (see equation (6)) is shown when the system of 100 spirals is in its lowest-energy

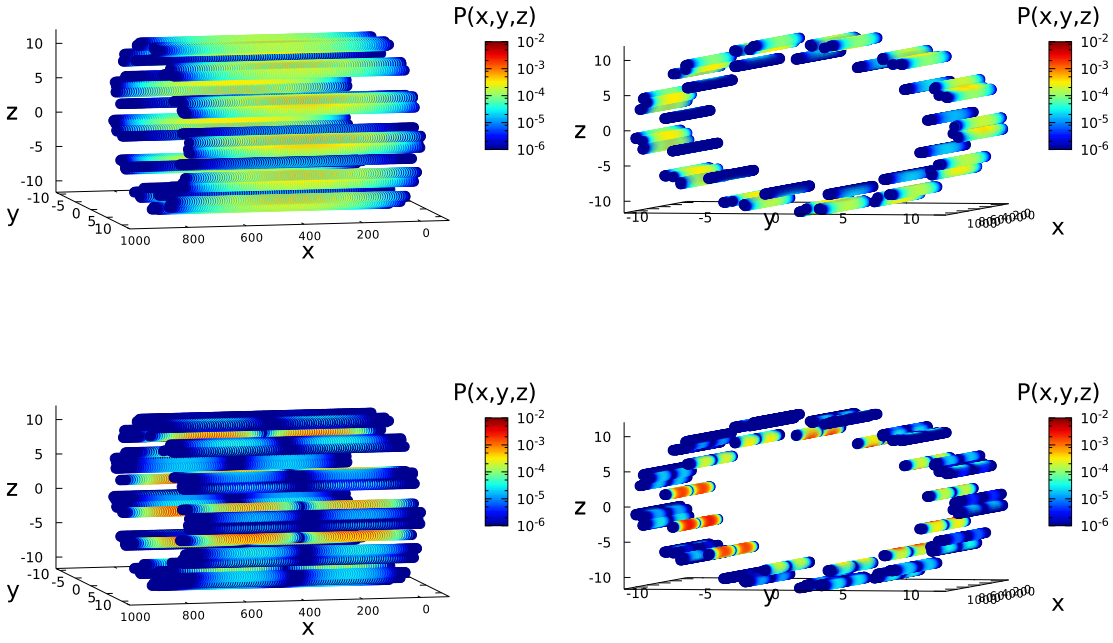

Figure 4. *Superradiant and subradiant excitonic states in a microtubule.* The probability $P(x, y, z) = |\psi|^2$ of finding the exciton on a tryptophan chromophore of a microtubule segment of 100 spirals with 10 400 tryptophan molecules, is shown for the extended superradiant lowest exciton state (upper panels, lateral view (left) and in cross section (right)) and the most subradiant state (lower panels, lateral view (left) and in cross section (right)), which has the smallest decay width ($\Gamma/\gamma \simeq 10^{-8}$) and an energy in the middle of the spectrum ($E - e_0 = 2.1$ cm^{-1}). Lengths on each axis are expressed in nanometers. The participation ratio from equation (12) for the superradiant state in the upper panels is 3 512.92, and the participation ratio for the most subradiant state in the lower panels is 766.64.

state. One can see that this state represents a fully extended excitonic state over the whole microtubule segment, and thus it could be capable of supporting ultra-efficient transport of photoexcitation. Note that the superradiant lowest exciton state is the state which is most strongly coupled to the electromagnetic field (highest decay width), and thus the fact that it represents an extended state implies that the absorbed photon will be shared by many tryptophan molecules in a coherent way, at least up to the dephasing time. In the lower panels of figure 4, we also show for comparison the most subradiant state for a microtubule of 100 spirals. Note that in this case the excitation probability is concentrated on the chromophores of the inner wall of the microtubule lumen, contrary to the superradiant state where the excitation probability is delocalized on the chromophores of the external wall that forms an interface with the cytoplasm.

3.1. Structure of the superradiant lowest exciton state, super and subtransfer processes

In order to understand the structure of the superradiant lowest exciton state of a large microtubule segment, we now project the lowest exciton state of the whole structure $|\psi_{gs}\rangle$ not on the site basis as we did in figure 4, but instead onto alternative basis states: a basis $|\phi_m\rangle$ made of the eigenstates of a group of 13 coupled spirals. The idea is to take a microtubule segment which we can divide in multiples of 13 spirals and analyze which eigenstates of a block of 13 spirals contribute to form the superradiant lowest exciton state of the whole microtubule. Note that 13 is the minimum number of spirals we need to have a superradiant lowest exciton state (see figure 2), and each block is made of $n_B = 104 \times 13 = 1352$ states. If we call $|\psi_q^s\rangle$ the eigenstate q of the s block of 13 spirals, then the basis state $|\psi_m\rangle = |\psi_q^s\rangle$ for $(s-1)n_B < m \leqslant sn_B$ while $|\psi_m\rangle = 0$ for $m > sn_B$ or $m \leqslant (s-1)n_B$. In the upper panel of figure 5, the first $13 \times 104 = 1352$ states correspond to the eigenstates of the first 13 coupled spirals, the second 13×104 states correspond to the eigenstates of the coupled spirals from 14 to 26, and so on. As one can see from figure 5, the components of the lowest exciton state over the 13 coupled spirals eigenstates are mainly concentrated in the lowest exciton states of each block of 13 coupled spirals (see also inset of figure 5 upper panel). The result in figure 5 clearly shows that the lowest exciton state of the whole structure mainly consists of a superposition of lowest exciton states of smaller blocks of spirals. This non-trivial result arises from the symmetry of the systems, see discussion in [37]. A very interesting consequence of this is that the total lowest exciton state emerges from coupling between the lowest exciton states of smaller blocks. Such coupling is of a supertransfer kind as we show below.

The supertransfer coupling [4] between the lowest exciton states of smaller blocks originates from the interaction of the giant dipole moments associated with the superradiant lowest exciton states of each block of 13 spirals. Indeed, the lowest exciton state of a block of 13 coupled spirals has a decay rate which is ~235 times larger

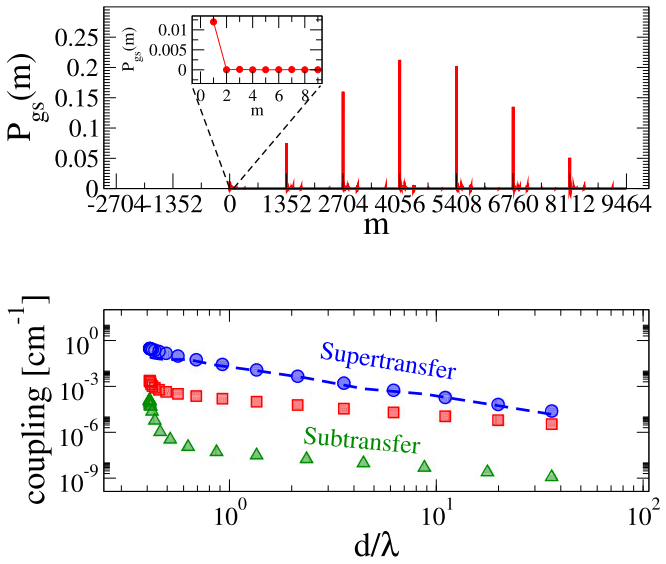

Figure 5. Upper panel: projection of the lowest exciton state $|\psi_{gs}\rangle$ of a microtubule segment of 91 spirals over the basis states $|\phi_m\rangle$ built from the eigenstates of blocks of 13 spirals within the segment (see text). The basis states, indexed by m, are ordered from low to high energy in each block ($13 \times 104 = 1352$ states). The projection has been computed as $P_{gs}(m) = |\langle\phi_m|\psi_{gs}\rangle|^2/\sum_m|\langle\phi_m|\psi_{gs}\rangle|^2$. The inset, zooming in on the first nine eigenstates of the first block, confirms that the lowest exciton state of the whole microtubule segment can be viewed as a coherent superposition of the lowest exciton states of the smaller blocks of spirals. Lower panel: coupling between the superradiant lowest exciton states of two blocks of 13 spirals (blue circles) is compared with the average pairwise coupling between the chromophores of each block (red squares) and the most subradiant states of the two blocks (green triangles). The couplings are plotted versus the distance d/λ (normalized by the excitation wavelength $\lambda = 280$ nm) between the centers of the two blocks. When two blocks are immediate neighbors, the center-to-center distance is $d \approx 116$ nm. The supertransfer interaction between the giant dipoles of the lowest exciton states of the two blocks (see equation (11)), valid for large inter-block distances d, is shown as a blue dashed curve.

than the single-molecule decay rate. In order to prove the previous statement, let us compute the coupling between the eigenstates of two blocks of 13 coupled spirals, say block 1 and block 2. We will compute the coupling as a function of the distance between the two blocks, assuming the blocks are translated along the principal cylinder axis. Let us indicate the two corresponding qth eigenstates of the two blocks as

$$|\psi^{s,q}\rangle = \sum_k C_k^{s,q}|k\rangle,$$

where the states $|k\rangle$ represent the site basis of a block and $s = 1, 2$. The coupling between two single block eigenstates can be written as

$$V_{12}^q = \langle\psi^{1,q}|V|\psi^{2,q}\rangle = \sum_{k,k'}(C_k^{1,q})^* C_{k'}^{2,q} V_{k,k'}. \tag{8}$$

Note that $\langle\psi^{1,q}|$ is not the complex conjugate of $|\psi^{2,q}\rangle$ but the transpose of it, as we explain in section 2. Using equations (1), (4), and (5), we have that $V_{k,k'} = \Delta_{k,k'} - i\Gamma_{k,k'}/2 = f(r_{k,k'})\vec{\mu}_k \cdot \vec{\mu}_{k'} + g(r_{k,k'})$ $(\vec{\mu}_k \cdot \hat{r}_{k,k'})(\vec{\mu}_{k'} \cdot \hat{r}_{k,k'})$, where the functions f, g can be derived from equations (1), (4), and (5). When the distance between two blocks is much larger than their diameter we can approximate $r_{k,k'} \approx R_{12}$ where R_{12} is the distance between the centers of the two blocks. Equation (8) then becomes

$$V_{12}^q = \sum_{k,k'}(C_k^{1,q})^* C_{k'}^{2,q}[f(R_{12})\vec{\mu}_k \cdot \vec{\mu}_{k'} + g(R_{12})(\vec{\mu}_k \cdot \hat{R}_{12})(\vec{\mu}_{k'} \cdot \hat{R}_{12})], \tag{9}$$

where $\vec{\mu}_k$ is the dipole moment of the k molecule. The above expression can be re-written in terms of the dipole strength of the eigenstates. The transition dipole moment $\vec{D}_q$ associated with the qth eigenstate can be defined as follows:

$$\vec{D}_q = \sum_{i=1}^{N} C_{q,i}\,\vec{\mu}_i. \tag{10}$$

The dipole coupling strength (often referred to as simply the dipole strength) of the qth eigenstate is defined by $|\vec{D}_q|^2$ (note that due to normalization $\sum_{n=1}^{N}|\vec{D}_q|^2 = N$). Under the approximation that the imaginary part of the Hamiltonian (1) can be treated as a perturbation and $L/\lambda \ll 1$ we have $|\vec{D}_q|^2 \approx \Gamma_q/\gamma$ (see appendix B). Thus, using equations (9), (10) can be re-written as

$$V_{12}^q = [f(R_{12})|\vec{D}_q|^2 + g(R_{12})(\vec{D}_q \cdot \hat{R}_{12})(\vec{D}_q^* \cdot \hat{R}_{12})]. \tag{11}$$

As a result for the coupling between the lowest exciton states of blocks of 13 spirals, we obtain $V_{12}^{gs} \propto |D_{gs}|^2 \approx \Gamma_{gs}/\gamma \approx 235$, Γ_{gs}/γ is the decay with of the lowest exciton state of 13 spirals (note that we can use the $|D_{gs}|^2 \approx \Gamma_{gs}/\gamma$ approximation since for a block of 13 spirals we have $L/\lambda \approx 0.4$). The above expression represents the interaction between the giant dipoles of the lowest exciton states of each block. Therefore, states with a large dipole strength will have a supertransfer coupling proportional to the dipole strength of the eigenstates. Note that the coupling between eigenstates with a small dipole strength can give rise to a subtransfer effect, which has been shown in [37]. In the lower panel of figure 5, the coupling between the lowest exciton states with a large dipole strength (blue circles) and between the most excited states with a very small dipole strength (green triangles) of two blocks of 13 spirals is compared with the average coupling between the molecules of each block (red squares). Note that the lowest exciton state of a block of 13 spirals is the most superradiant state with $\Gamma/\gamma \approx 235$, while the highest-energy state is the most subradiant with the lowest decay width $\Gamma/\gamma \approx 10^{-6}$ for a block of 13 spirals. The couplings are shown as a function of the center-to-center distance between the two blocks normalized by the wavelength connected with the optical transition. One can see that the coupling between the lowest exciton states is significantly larger than the average coupling between the molecules. Moreover, for large center-to-center distances d, the coupling between the lowest exciton states is well-approximated by equation (11) (see blue dashed curve), thus proving the existence of a supertransfer effect. On the other hand, the coupling between the most excited states of the two blocks is much smaller than the average coupling between the molecules, showing a subtransfer effect. The above results suggest that the dynamics will be very dependent on the initial conditions and will exhibit at least two distinct timescales due to the presence of supertransfer and subtransfer processes. In the next section, we will show how the cooperativity-enhanced coupling between the lowest exciton states of blocks of spirals can boost photoexcitation transport.

4. Transport of photoexcitations via supertransfer

In this section we consider the spreading velocity of an initial excitation concentrated in the middle of a microtubule made of 99 spirals, with a total length of about 800 nm. The spreading of the initial excitation has been measured by the root-mean-square deviation (RMSD) of the excitation along the longitudinal axis of the microtubule. Given that the initial state of the system is described by the wavefunction $|\psi(0)\rangle$, the average position of the excitation on the axis of the microtubule can be computed with $\overline{Q}(t) = \sum_k |\langle k|\psi(t)\rangle|^2 z_k$, where z_k is the position of the kth molecule on the longitudinal axis and $|\psi(t)\rangle$ is the wavefunction at time t. Thus the variance as a function of time can be computed with $\sigma^2(t) = \sum_k |\langle k|\psi(t)\rangle|^2 z_k^2 - \overline{Q}(t)^2$, from which follows $\mathrm{RMSD}(t) = \sqrt{\sigma^2(t)}$.

We have chosen different initial conditions to show the effect of cooperativity on the spreading of the excitation: (i) an initial excitation concentrated on a single randomly selected site of the central spiral; and (ii) an initial excitation concentrated in the lowest exciton state of the central block of 5, 13, or 21 spirals. As displayed in figure 6, the spreading of the initial wave packet is always ballistic ($\mathrm{RMSD}(t) \propto t$) so that we can define a velocity of spreading V as the linear slope. Note that V increases as we increase the number of spirals over which the initial excitation is spread and then saturates when the number of spirals becomes large. Indeed from figure 6 we can see that the spreading velocity is the same when the initial state coincides with the lowest exciton state of 13 or 21 central spirals. When the excitation starts from the lowest exciton state of 21 central spirals, V is more than five times the velocity of an excitation concentrated on a single site. Such an effect is due to supertransfer coupling between the lowest exciton states of blocks of spirals, and as a consequence of the fact that the lowest exciton states of the central spirals have a large overlap with the extended superradiant state of the whole microtubule, as shown in figure 5.

For comparison we also estimated the spreading velocity of an excitation which can be expected based on the typical nearest-neighbor coupling present in the system. In the Trp case the typical nearest-neighbor coupling is $J \approx 50\ \mathrm{cm}^{-1}$, so that the time needed for the excitation to move by one Trp can be estimated as $\tau = 1/(4\pi cJ) \approx 0.053$ ps, where the light velocity is $c \approx 0.03\ \mathrm{cm\ ps}^{-1}$. This can be derived from the period of oscillation between two sites at resonance, which is given by $T = \hbar/J' = hc/(2\pi cJ')$, and $\tau = T/2$ (note that $J = J'/(hc)$ is the coupling in cm^{-1} as measured in this paper). The average distance between Trps projected along the main axis of the microtubule can be evaluated from $d = 810\ \mathrm{nm}/10\,400 = 0.078$ nm. We thus obtain a velocity $V_{NN} = d/\tau \approx 1.47$ nm/ps, which is shown by the black dashed line in figure 6. Note that V_{NN} is about two times smaller than the spreading velocity starting from a single site. This is probably due to the fact that the long-range interactions between the sites favor the spreading of the excitation (see section 5). Most importantly, V_{NN} is about ten times smaller then the spreading velocity of a delocalized excitation obtained by setting the initial state equal to the lowest exciton state of 13 or more central spirals. This strong dependence on initial

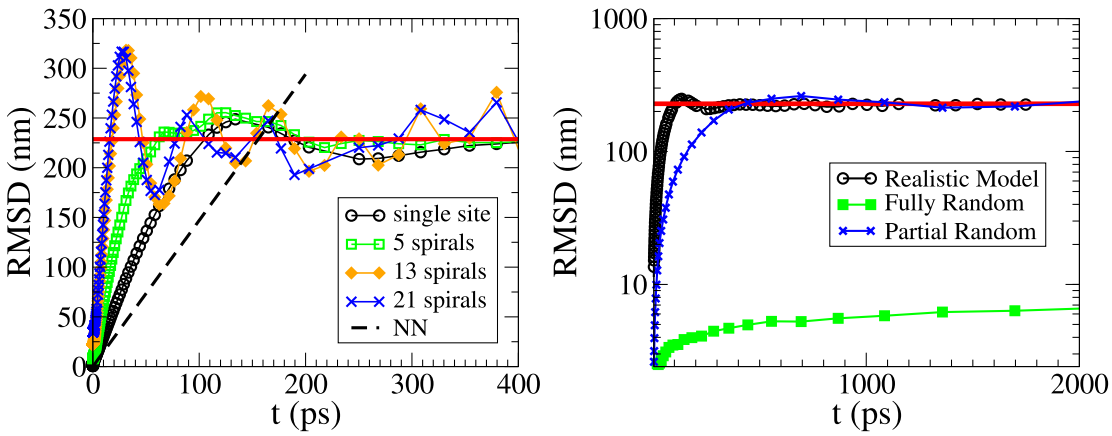

Figure 6. Root-mean-square deviation (RMSD) as a function of time for an initial excitation concentrated in the middle of a microtubule comprised of 99 spirals with a total length of about 810 nm. Left panel: the case of an initial excitation concentrated on a single site of the central spiral (black circles) is compared with an initial condition on the lowest exciton state of the central five (empty green squares), 13 (orange crosses), and 21 (blue stars) spirals. For comparison, the spreading expected from the strength of the nearest-neighbor coupling is also shown (black dashed line) and described in the text. The equilibrium value for an excitation equally distributed over all the tryptophans of the microtubule is shown as a red horizontal line. The spreading velocity of an excitation starting from a single site is about two times faster than the spreading associated with the amplitude of the nearest-neighbor coupling (NN velocity), while the spreading velocity of an excitation which starts in the lowest exciton state of more than 13 spirals is about ten times faster than the NN velocity. Right panel: here the case of an initial excitation concentrated on a single site of the central spiral is considered for three different models—the realistic model (black circles and same data as in the left panel), the fully random model where all the dipoles are randomly oriented (filled green squares), and the partial random model where the dipoles are oriented at random but repeated in the same configuration for all spirals (blue crosses).

conditions might also explain the variety of experimental data obtained for diffusive excitonic behavior in molecular nanotubes.

For large times, the RMSD reaches a stationary value that assumes the excitation becomes equally distributed on all Trps of the microtubule. We can compute such a stationary value of the RMSD from the positions of the Trps, by setting $\overline{Q} = \sum_k z_k/N$ and $\sigma^2 = \sum_k z_k^2/N - \overline{Q}^2$, so that RMSD $= \sqrt{\sigma^2}$. For a microtubule made of 99 spirals we obtain RMSD ≈ 228 nm. This value is shown in figure 6 as a horizontal red line, and it agrees very well with the numerical results.

In real microtubules it can be the case that, due to various decorations on the structure of the lattice (including other interacting proteins and nucleotide di- and tri-phosphates, for example), a localized excitation could occur. In addition, due to the presence of ultraweak light-emitting molecules called reactive oxygen species—the products of aerobic respiration in all biological cells—such excitations can indeed be localized on individual chromophores of the microtubule due to proximity. A fuller description of these light-emitting molecules and their impact on tubulin polymers is given in [26]. We would also like to emphasize that a photon is likely to be absorbed by the superradiant state of a block of spirals, since the superradiant state is the state which is most strongly coupled to the electromagnetic field (i.e. it has the highest decay width and absorption rate). For this reason an initial excitation coinciding with the superradiant state of a block of microtubule spirals is well motivated, and the fact that its spreading is enhanced can have important consequences for photoexcitation transport.

Finally, in order to emphasize the role of symmetry in the transport properties of the system, in the right panel of figure 6 we show the spreading of an initial excitation starting from a single site on the central spiral for the realistic model considered before (black circles in both left and right panels represent the same data), for the fully random model, and for the partial random model. In both the latter models, the positions of the dipoles are kept fixed with respect to the realistic model, but the orientation of their dipoles has been randomized. Note that in the fully random model the dipole directions have been randomized along the entire microtubule length, whereas for the partial random model we have randomized the dipole orientations in one spiral and then repeated this configuration in all other spirals. For the partial random model, the excitation spreads over the whole microtubule segment with a smaller velocity than the realistic model, while for the fully random model the spreading is extremely slow and remains well below the value (see horizontal red line) of an equally distributed excitation during the whole simulation time. The above results show the relevance of native symmetry in excitonic energy transport through the microtubule. We would like to point out that several recent works have highlighted the role of symmetry in enhancing coherent [37] and transport properties of molecular networks [49].

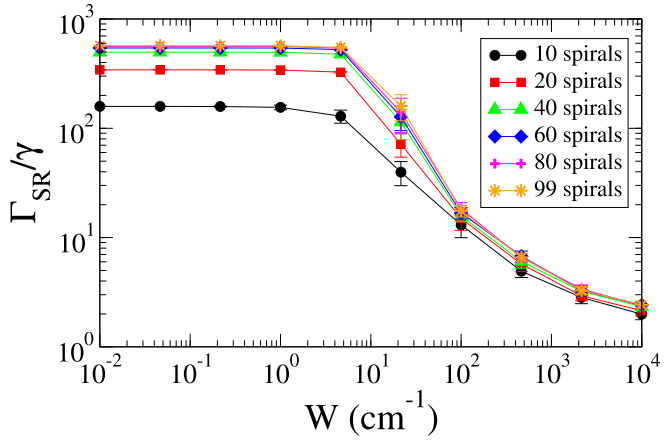

Figure 7. Normalized decay width of the superradiant state is plotted versus the strength of static disorder W for a microtubule segment of different lengths.

5. Robustness to disorder and the role of long-range interactions

In order to study the robustness to disorder of the superradiant lowest exciton state, we have analyzed the system in the presence of static disorder, i.e. time-independent and space-dependent fluctuations of the excitation energies of the tryptophans comprising the microtubule chromophoric lattice. Specifically we consider that the excitation energies of the tryptophans are uniformly distributed around the initial value e_0, between $e_0 - W/2$ and $e_0 + W/2$, so that W represents the strength of the static disorder. It is well known that static disorder induces localization of the eigenstates of a system, a phenomenon known as Anderson localization [50]. Due to such localization, for each eigenstate the probability of finding the excitation is concentrated on very few sites for large disorder, and only on one site for extremely large disorder. Note that Anderson localization usually occurs in the presence of short-range interactions, but in our model there are multiple contributions from a complicated power law for the interaction (see equation (4)), so that the results of our analysis are not obvious.

In order to study the robustness of superradiance to disorder, we plot in figure 7 the maximum normalized decay width Γ_{SR}/γ as a function of the disorder strength W, using the full realistic non-Hermitian Hamiltonian given in equation (1) for different microtubule sizes. Note that the most superradiant state (i.e. largest decay width) coincides with the lowest exciton state of the microtubule for sizes of 13 or more spirals. One can see that the disorder at which the width of the superradiant state starts to decrease is independent of the system size (within the system sizes considered in our simulations). This is quite surprising for quasi-one dimensional structures, which usually exhibit a critical disorder that decreases as the system size grows [51]. Indeed, for short-range interactions in quasi-one dimensional structures, the critical static disorder strength W_{cr} needed to localize the system goes to zero as the system size goes to infinity, with $W_{cr} \propto J/\sqrt{N}$.

In order to understand how the above results could be explained by the effective range of the interaction, we have compared our realistic model which contains long-range interactions with the same model where the long-range interactions have been suppressed. Specifically the short-range model has been obtained by considering only the interactions between Trps with a center-to-center separation less than 4 nm. In order to perform such a comparison, only the Hermitian part of the realistic model Hamiltonian given in equation (1) has been taken into account. We considered only the Hermitian part of the Hamiltonian because it constitutes a good approximation of the whole Hamiltonian (see discussion in appendix B) and, most importantly, allows for comparison of different ranges of interaction. Indeed, in the full non-Hermitian model we cannot change the range of the interaction without introducing inconsistencies (i.e. negative decay widths). Below we will show that the results thus obtained are consistent with the analysis of the whole Hamiltonian given in figure 7, where the full non-Hermitian Hamiltonian has been considered.

We analyzed the effect of disorder for the two different models (long-range and short-range) through the participation ratio (PR)

$$\mathrm{PR} = \left\langle \sum_i |\langle q_i|\psi\rangle|^2 \Big/ \sum_i |\langle q_i|\psi\rangle|^4 \right\rangle \tag{12}$$

of the eigenstates $|\psi\rangle$ of the system, where the large outer brackets, $\langle ... \rangle$, stand for the ensemble average over different realizations of the static disorder. The PR is widely used to characterize localization properties [52], and

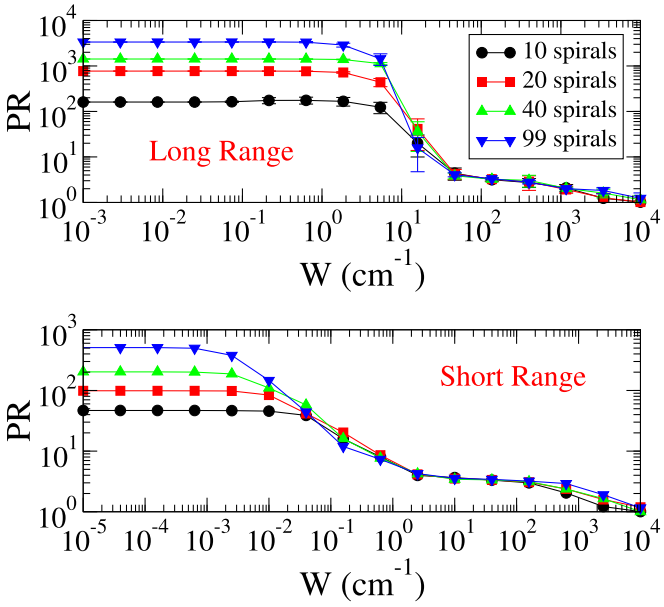

Figure 8. Participation ratio (PR) of the lowest exciton state for a microtubule of different lengths is shown versus the strength of static disorder W, averaged over ten realizations of disorder for each system length. The upper panel presents the results of the full model, where the interaction between the tryptophans has a long-range nature (see equation (1)). However, note that only the Hermitian part of the Hamiltonian in equation (1) has been used to obtain the data shown in both panels of this figure. In the lower panel, the PR of the lowest exciton state for a microtubule of different lengths is shown versus the strength of static disorder W for the case of short-range interactions only, considering only the couplings between tryptophans with a center-to-center separation smaller than 4 nm.

it satisfies the bounds $1 \leqslant \mathrm{PR} \leqslant N$. For extended states, it increases proportionally to the system size N, while, for localized states, it is independent of N.

In order to study the effect of static disorder, we have analyzed the PR of the lowest exciton state as a function of the disorder strength W in figure 8. As shown in the upper panel of figure 8, where the long-range model is analyzed, the critical disorder at which the PR starts to decrease appears to be independent of the microtubule length. The critical disorder obtained in this case is consistent with the analysis of the critical disorder needed to quench superradiance as shown in figure 7. The response of the system to disorder is completely different for the short-range model. The robustness to disorder of the lowest exciton state of such a model is shown in the lower panel of figure 8. As one can see, the critical disorder decreases with the system size in this case, as would be expected for quasi-one dimensional systems with short-range interactions. The difference between the two panels of figure 8 shows that the long-range nature and symmetry of the interactions play a very significant role in enhancing the robustness of excitonic states in microtubules to disorder. However, we note that robustness to disorder could also be connected to supertransfer, and not only to the long-range of the interaction. For further details see the discussion in [37] and in appendix C.

6. Conclusions and perspectives

We have analyzed the excitonic response of microtubules induced by the coupling of tryptophan molecules, which are the most strongly photoactive molecules in the spiral-cylindrical lattice. The positions and orientations of the dipoles of the tryptophan molecules have been obtained in previous works by molecular dynamics simulations and quantum chemistry calculations and have closely reproduced experimental spectra for the tubulin heterodimeric protein [26]. Analyzing the properties of a microtubule of length $L \sim 800$ nm, which is larger than the wavelength of the excitation transition ($L > \lambda = 280$ nm), requires an approach that goes beyond the transition dipole–dipole couplings alone. This is why we take into consideration radiative interactions containing non-Hermitian terms.

Our analysis has shown that the coupling between tryotophan molecules is able to create a superradiant lowest exciton state, similar to the physical behavior of several photosynthetic antenna systems. Such a superradiant lowest exciton state, which absorbs in the UV spectral range, has been shown to be a coherent excitonic state extended over the whole microtubule lattice of tryptophan molecules. Interestingly, the superradiant lowest exciton state appears to be delocalized on the exterior wall of the microtubule, which interfaces with the cytoplasm, suggesting the possibility that these extended but short-lived (few picosecond) excitonic states may be involved in communication with cellular proteins that bind to microtubules in order to

carry out their functions. At the same time, we have shown that long-lived (hundreds of milliseconds) subradiant states can be concentrated on the inner wall of the microtubule lumen. These subradiant states could be particularly important in the synchronization of neuronal processes in the brain, where microtubules can extend to the micron scale and beyond.

Moreover, we have shown that the superradiant lowest exciton state of the whole microtubule arises through a supertransfer coupling between the lowest exciton states of smaller blocks of spirals within the microtubule. For this reason, microtubule superradiance is essentially an emergent property of the whole system that develops as 'giant dipole' strengths of superradiant lowest exciton states of constituent blocks interact to form a delocalized coherent state on the entire structure. This is a hallmark of self-similar behavior, in the sense that subunit blocks of spirals exhibit superradiant characteristics that recapitulate roughly what is seen in the whole. Only by considering the entire structure (or at least a substantial fraction of the spirals) do we uncover cooperative and dynamical features of the system that would otherwise fail to be captured in more reductionist models. Supertransfer coupling between excitonic states of different blocks of spirals in the microtubule segment is critical to the manifestation of these cooperative behaviors and explains the calculated couplings to excellent agreement.

Such supertransfer coupling is able to enhance the spreading of photoexcitation inside the microtubule. The spreading of photoexcitation is ballistic, despite the fact that the native dipole orientations of the tryptophan molecules are not fully symmetric even in the absence of static disorder (see figure 1). The spreading velocity is strongly dependent on the initial conditions, and, due to supertransfer, it can be about ten times faster than the velocity expected from the amplitude of the nearest-neighbor coupling between the tryptophan molecules in such structures. These results show that the characteristic supertransfer processes analyzed in photosynthetic antenna complexes may also be present in microtubules.

Finally, we have analyzed the robustness of microtubule superradiance to static disorder. We have shown that the symmetry and long-range nature of the interactions give an enhanced robustness to such structures with a critical disorder which appears to be independent of the system size (up to the system sizes analyzed in this paper). This is at variance with what usually happens in quasi-one dimensional structures with short-range interactions, where the critical disorder W_{cr} goes to zero as the system size grows. Indeed, for quasi-one dimensional systems with short-range interactions only, we have $W_{cr} \propto J/\sqrt{N}$, where J is the nearest-neighbor coupling and N is the number of chromophore sites. The critical disorder at which superradiance and the delocalization of the lowest exciton state are precipitously affected is found to be on the order of 10 cm^{-1} (see figure 8). Such a value of disorder is not extremely large, as natural disorder can be on the order of kT, ranging from 50 to 300 cm^{-1}. Still, such critical disorder is much larger than the critical disorder expected from the typical nearest-neighbor coupling between tryptophan molecules. Such enhanced robustness to static disorder as a result of long-range interactions and symmetry can greatly increase diffusion lengths and thereby support ultra-efficient photoexcitation transport.

To refine our studies, future work should certainly include consideration of the other photoactive amino acids, such as the aromatics tyrosine and phenylalanine, that are present in microtubules, as well as the effects of thermal relaxation on coherent energy transport. To realistically take into account such environmental effects, we must analyze the role of out-of-equilibrium processes, which can dominate the dynamics of the proper functioning state of the microtubule before thermalization. Environmental decoherence will be considered explicitly in a future work. Our contribution in this paper is to provide a first analysis and motivation for such further nuanced studies of excitonic states in this intriguing and highly symmetric biological system.

The significance of photoexcitation transport in microtubules is an open question in the biophysics community, and further experimental and theoretical works are needed to establish the precise mechanisms of their optical functionality. Our results point towards a possible role of superradiant and supertransfer processes in microtubules. Both cooperative effects are able to induce ultra-efficient photoexcitation absorption and could serve to enhance energy transport over long distances under natural conditions. We hope that our results will inspire further experimental studies on microtubules to gather evidence for UV superradiance in such important biological structures.

It would be interesting to further contextualize the biological implications of our results. In a series of studies spanning a period of almost a quarter century, Albrecht-Buehler observed that living cells possess a spatial orientation mechanism located in the centrosome [35, 53–55]. The centrosome is formed from an intricate arrangement of microtubules in two perpendicular sets of nine triplets (called centrioles). This arrangement provides the cell with a primitive 'eye' that allows it to locate the position of other cells within a two-to-three-degree accuracy in the azimuthal plane and with respect to the axis perpendicular to it [55]. Though it is still a mystery how the reception of electromagnetic radiation is accomplished by the centrosome, superradiant behavior in these microtubule aggregates may play a role.

Acknowledgments

GLC acknowledges the support of PRODEP (511-6/17-8017). TJAC would like to acknowledge financial support from the Department of Psychology and Neuroscience and the Institute for Neuro-Immune Medicine at Nova Southeastern University (NSU), and work in conjunction with the NSU President's Faculty Research and Development Grant (PFRDG) program under PFRDG 335426 (Craddock PI). PK was supported in part by the National Institute on Minority Health and Health Disparities of the National Institutes of Health under Award Number G12MD007597. The content is solely the responsibility of the authors and does not necessarily represent the official views of the National Institutes of Health. PK would also like to acknowledge support from the US-Italy Fulbright Commission and the Whole Genome Science Foundation.

Appendix A. Microtubule tryptophan dipole positions and orientations

The tubulin α–β heterodimer structure was obtained by repairing the protein data bank (PDB: www.rcsb.org) [56] structure 1JFF [57] by adding missing residues from 1TUB [58] after aligning 1TUB to 1JFF. This initial repaired dimer structure was oriented by itself alone such that the (would be) protofilament direction aligned with the x-axis, the normal to the (would be) outer microtubule surface aligned with the y-axis, and the direction of (would be) lateral contacts aligned with the z-axis, before subsequent translation and rotation. A single spiral of 13 tubulin dimers was generated by translating each dimer 11.2 nanometers (nm) in the y-direction, then successively rotating the resulting dimer structure by multiples of -27.69° in the y–z plane about the origin around the x-axis, and successively shifting each dimer by multiples of 0.9 nanometers in the x-direction. This resulted in a left-handed helical-spiral structure with a circular radius of 22.4 nm passing through the center of each dimer in the B-lattice microtubule geometry described by Li *et al* [59] and Sept *et al* [60]. The orientation of the $1L_a$ excited state of each tryptophan molecule in the resulting structure was taken as 46.2° above the axis joining the midpoint between the CD2 and CE2 carbons of tryptophan and carbon CD1, in the plane of the indole ring (i.e. towards nitrogen NE1). The Cartesian positions and unit vector directions of the 104 tryptophans of the first spiral are given in table A1 below. To generate successive spirals, the initial spiral coordinates were translated along the x (i.e. protofilament) direction by multiples of 8 nm. Modeling was done with PyMOL 1.8.6.2 [61].

Table A1. First spiral dipole positions (Å) and unit vectors.

x	y	z	$\hat{\mu}_x$	$\hat{\mu}_y$	$\hat{\mu}_z$
−2.378	103.218	14.720	−0.701 14	0.665 10	−0.256 99
−13.691	123.899	7.109	0.654 56	−0.702 98	−0.278 16
13.384	124.916	−9.487	−0.538 55	−0.005 10	−0.842 58
−28.566	122.415	5.686	−0.185 73	-0.217 51	−0.958 22
6.622	97.563	−31.783	−0.701 25	0.469 22	−0.536 74
−4.691	112.339	−48.133	0.654 55	−0.751 73	0.080 39
22.384	105.527	−63.300	−0.538 54	−0.395 97	−0.743 76
−19.566	110.363	−48.703	−0.185 68	−0.638 15	−0.747 18
15.622	70.946	−70.331	−0.701 34	0.165 74	−0.693 29
4.309	76.431	−91.675	0.654 56	−0.628 18	0.420 64
31.384	63.350	−101.939	−0.538 42	−0.696 43	−0.474 43
−10.566	74.417	−91.261	−0.185 63	−0.912 28	−0.365 09
24.622	29.463	−92.094	−0.701 42	−0.175 12	−0.690 90
13.309	24.401	−113.542	0.654 55	−0.360 84	0.664 35
40.384	8.049	−116.552	−0.538 45	−0.837 15	−0.096 15
−1.566	22.810	−112.239	−0.185 84	−0.977 46	0.100 22
33.622	−17.382	−92.086	−0.701 21	−0.476 30	−0.530 52
22.309	−31.831	−108.725	0.654 55	−0.010 98	0.755 94
49.384	−47.710	−103.791	−0.538 40	−0.786 05	0.303 74
7.435	−32.636	−106.832	−0.185 61	−0.818 78	0.543 27
42.622	−58.858	−70.309	−0.701 12	−0.668 44	−0.248 25
31.309	−79.384	−78.327	0.654 55	0.341 93	0.674 27
58.384	−91.151	−66.579	−0.538 40	−0.554 61	0.634 45
16.435	−79.217	−76.278	−0.185 81	−0.472 52	0.861 51
51.622	−85.462	−31.752	−0.701 43	−0.706 94	0.090 67
40.309	−107.363	−29.312	0.654 56	0.616 02	0.438 25
67.384	−112.323	−13.442	−0.538 47	−0.196 91	0.819 32
25.435	−106.263	−27.576	−0.185 98	−0.018 12	0.982 39

Table A1. (Continued.)

x	y	z	$\hat{\mu}_x$	$\hat{\mu}_y$	$\hat{\mu}_z$
60.622	−91.101	14.753	−0.701 19	−0.584 26	0.408 63
49.309	−109.360	27.091	0.654 54	0.749 18	0.101 53
76.384	−106.376	43.448	−0.538 46	0.206 79	0.816 88
34.435	−107.578	28.118	−0.185 79	0.440 42	0.878 36
69.622	−74.482	58.551	−0.701 22	−0.327 15	0.633 46
58.309	−84.916	77.961	0.654 57	0.710 67	−0.257 84
85.384	−74.672	91.058	−0.538 50	0.562 68	0.627 23
43.435	−82.861	78.042	−0.185 66	0.798 24	0.573 01
78.622	−39.413	89.609	−0.701 01	0.004 58	0.713 13
67.309	−39.631	111.644	0.654 60	0.509 89	−0.558 14
94.384	−24.474	118.481	−0.538 46	0.789 61	0.294 24
52.435	−37.774	110.761	−0.185 83	0.973 05	0.136 53
87.622	6.073	100.812	−0.701 34	0.335 63	0.628 87
76.309	16.121	120.425	0.654 58	0.191 39	−0.731 37
103.384	32.718	119.434	−0.538 49	0.835 84	−0.106 78
61.435	17.355	118.780	−0.185 56	0.924 97	−0.331 68
96.622	51.555	89.594	−0.701 37	0.589 28	0.401 04
85.309	69.566	102.291	0.654 56	−0.170 71	−0.736 49
112.384	83.802	93.700	−0.538 47	0.690 44	−0.483 05
70.435	69.894	100.261	−0.185 84	0.665 06	−0.723 30
105.622	86.614	58.524	−0.701 31	0.708 20	0.081 38
94.309	108.463	61.397	0.654 56	−0.493 12	−0.573 04
121.384	117.076	47.174	−0.538 52	0.387 15	−0.748 41
79.435	107.810	59.447	−0.185 62	0.252 46	−0.949 64
39.057	102.384	14.619	−0.017 22	−0.525 00	0.850 93
53.331	124.899	−8.386	−0.683 14	0.492 02	−0.539 67
36.453	121.233	−4.011	0.988 86	0.147 94	0.016 63
12.616	122.434	5.625	−0.190 86	−0.224 02	−0.955 71
48.057	96.778	−31.485	−0.016 90	−0.069 07	0.997 47
62.331	106.023	−62.318	−0.683 15	0.184 96	−0.706 47
45.453	104.810	−56.739	0.988 82	0.138 86	−0.054 37
21.616	110.352	−48.767	−0.190 62	−0.642 62	−0.742 10
57.057	70.389	−69.702	−0.016 92	0.402 17	0.915 41
71.331	64.247	−101.300	−0.683 15	−0.164 73	−0.711 46
54.453	65.765	−95.796	0.988 82	0.097 92	−0.112 49
30.616	74.376	−91.313	−0.190 47	−0.913 72	−0.358 93
66.057	29.262	−91.278	−0.017 30	0.781 43	0.623 76
80.331	9.139	−116.402	−0.683 14	−0.476 49	−0.553 42
63.453	13.041	−112.235	0.988 85	0.034 27	−0.144 94
39.616	22.750	−112.267	−0.190 77	−0.975 79	0.106 98
75.057	−17.181	−91.270	−0.017 07	0.981 86	0.188 83
89.331	−46.675	−104.165	−0.683 12	−0.679 18	−0.268 45
72.453	−41.283	−102.288	0.988 85	−0.037 02	−0.144 22
48.616	−32.701	−106.829	−0.190 59	−0.814 21	0.548 39
84.057	−58.300	−69.680	−0.017 07	0.957 20	−0.288 91
98.331	−90.408	−67.392	−0.683 09	−0.726 12	0.078 34
81.453	−84.762	−68.236	0.988 89	−0.099 73	−0.110 25
57.616	−79.273	−76.244	−0.190 47	−0.466 22	0.863 92
93.057	−84.676	−31.454	−0.017 21	0.713 39	−0.700 55
107.331	−112.043	−14.506	−0.683 10	−0.606 69	0.406 58
90.453	−107.435	−17.878	0.988 81	−0.140 01	−0.051 60
66.616	−106.297	−27.520	−0.190 64	−0.011 55	0.981 59
102.057	−90.266	14.651	−0.017 06	0.305 98	−0.951 89
116.331	−106.622	42.375	−0.683 16	−0.348 62	0.641 68
99.453	−104.109	37.249	0.988 80	−0.148 00	0.019 35
75.616	−107.582	28.183	−0.190 53	0.445 82	0.874 61
111.057	−73.790	58.073	−0.017 08	−0.171 42	−0.985 05
125.331	−75.389	90.223	−0.683 11	−0.009 97	0.730 25
108.453	−75.546	84.516	0.988 84	−0.121 78	0.085 77
84.616	−82.834	78.102	−0.190 55	0.801 45	0.566 89
120.057	−39.023	88.865	−0.017 03	−0.609 39	−0.792 69
134.331	−25.497	118.074	−0.683 14	0.330 05	0.651 45
117.453	−28.288	113.094	0.988 88	−0.067 76	0.132 36

Table A1. (Continued.)

x	y	z	$\hat{\mu}_x$	$\hat{\mu}_y$	$\hat{\mu}_z$
93.616	−37.723	110.802	−0.190 64	0.973 06	0.129 64
129.057	6.073	99.971	−0.017 07	−0.908 05	−0.418 51
143.331	31.624	119.550	−0.683 13	0.595 19	0.423 18
126.453	26.838	116.437	0.988 91	0.001 53	0.148 53
102.616	17.419	118.792	−0.190 54	0.921 88	−0.337 38
138.057	51.164	88.850	−0.017 32	−0.998 53	0.051 31
152.331	82.887	94.311	−0.683 12	0.723 71	0.097 98
135.453	77.203	93.780	0.988 88	0.070 31	0.131 06
111.616	69.956	100.242	−0.190 74	0.659 33	−0.727 26
147.057	85.922	58.046	−0.017 08	−0.860 20	0.509 68
161.331	116.549	48.140	−0.683 14	0.686 44	−0.249 26
144.453	111.269	50.311	0.988 85	0.123 36	0.083 42
120.616	107.856	59.401	−0.190 53	0.245 75	−0.950 42

Appendix B. Comparison between dipole–dipole and radiative Hamiltonians

Here we compare the dipole–dipole Hamiltonian (Dipole model), which includes only the Hermitian part of the coupling in equation (7), with the full radiative non-Hermitian Hamiltonian given in equations (1)–(5) (nH model). We will also include in our analysis the Hermitian part of the full radiative non-Hermitian Hamiltonian (H model). For the three models (Dipole, nH, and H) we compare both the real-valued energies and the dipole coupling strengths of their eigenstates. We will show that, in the small-volume limit $L/\lambda \ll 1$, both quantities can be computed with the three models, but when the system size is larger than the wavelength, only the nH model can be used to compute the dipole strengths of the eigenstates. However, the H model still gives a close estimation to the nH model for the real energies in the large-volume limit, though the Dipole model displays deviations from the nH model values.

In figure B1, we compare the real part of the spectrum for the three models, focusing on the eigenvalues close to the lowest exciton state. In the upper panel, we present a microtubule made of only one spiral, so that $L/\lambda \ll 1$. In this case the three models all give very similar estimations of the eigenvalues. In the lower panel, the case of a microtubule of 100 spirals is considered. In this case the system size is not small compared with the wavelength, as $L/\lambda \approx 3$. One can see that while the H model is a very good approximation of the nH model, the Dipole model exhibits maximum deviations of $\sim 1\ \mathrm{cm}^{-1}$ at and near the lowest exciton state.

When the system size is small compared to the wavelength associated with the optical transition of the molecules, the optical absorption of an eigenstate of the aggregate can be estimated in terms of its dipole strength, computed only from the Hermitian part of the Hamiltonian (1). Denoting the nth eigenstate of the Hermitian part of the Hamiltonian (1) or of the Hamiltonian with only Hermitian coupling in (7) as $|E_n\rangle$, we can expand it in the site basis, so that

$$|E_n\rangle = \sum_{i=1}^{N} C_{ni}\ |i\rangle. \tag{B.1}$$

Note that the site basis is referred to by the tryptophan molecules and is composed of the states $|i\rangle$, each of them carrying a dipole moment $\vec{\mu}_i$. If N is the total number of molecules, then we will express the transition dipole moment $\vec{D}_n$ associated with the nth eigenstate as follows:

$$\vec{D}_n = \sum_{i=1}^{N} C_{ni}\ \hat{\mu}_i. \tag{B.2}$$

The dipole coupling strength (often referred to as simply the dipole strength) of the nth eigenstate is defined by $|\vec{D}_n|^2$ (note that due to normalization $\sum_{n=1}^{N}|\vec{D}_n|^2 = N$). Under the approximation that $L/\lambda \ll 1$ we have $|\vec{D}_n|^2 \approx \Gamma_n/\gamma$, where Γ_n is given by the imaginary part of the complex eigenvalues $\mathcal{E}_n = E_n - i\Gamma_n/2$ of the nH model. On the other hand, in the large-volume limit, the dipole as defined above in equation (B.2) gives incorrect results and does not represent the dipole of the eigenstates. This is shown in figure B2, where the maximum dipole strength computed using the Dipole model and the H model is compared with the maximum decay width $\Gamma_{\max}/\gamma$ computed with the full radiative nH model. As one can see, the dipole coupling strength computed as described above is valid only for small system sizes.

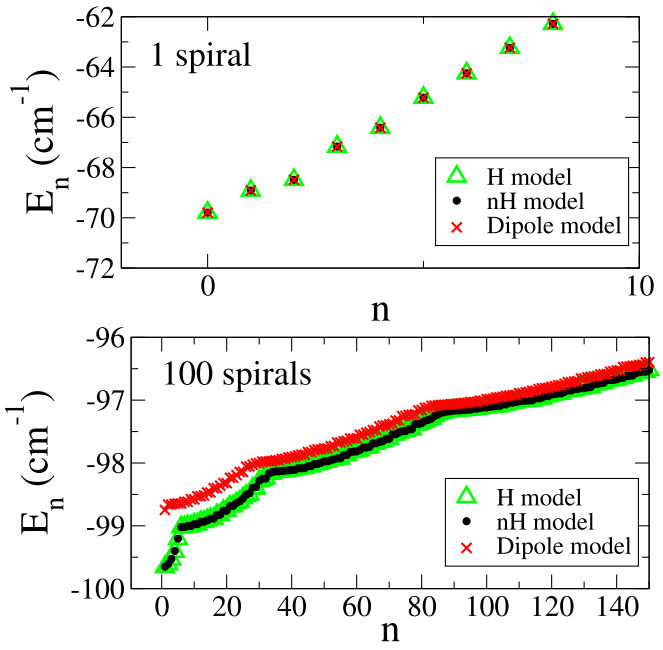

Figure B1. Lowest part of the spectrum (real-valued energies E_n versus eigenstate index n) for a microtubule of 1 spiral, $L/\lambda \ll 1$, (upper panel) and 100 spirals, $L/\lambda \approx 3$, (lower panel) is shown for the three different models considered (see main text). In the small-volume limit (upper panel), all three models give similar estimations of the spectrum, but in the large-volume limit (lower panel) the Dipole model deviates from the H and nH models, which are very close to each other.

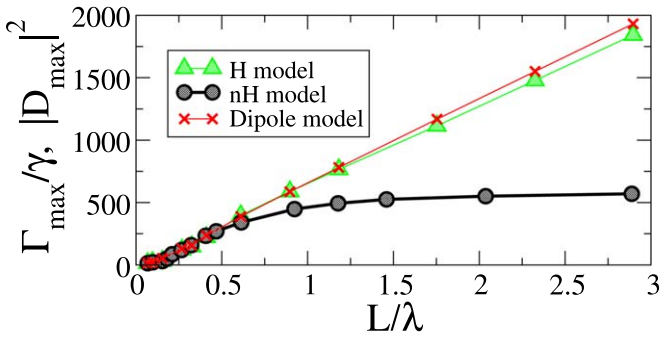

Figure B2. Maximum dipole coupling strength $|D_{\max}|^2$ computed from equation (B.2) for the Dipole and H models (see main text) is compared with the relative decay width $\Gamma_{\max}/\gamma$ computed from the full radiative nH model (see main text) as a function of the system size L normalized by the excitation wavelength ($\lambda = 280$ nm).

Appendix C. Supertransfer and the energy gap in the complex plane

We would like to point out that supertransfer might also play an important role in stimulating robustness to disorder. For instance, in figure C1 we show the energy differences in the complex plane between the lowest exciton state (which coincides with the most superradiant state for a microtubule of 13 or more spirals) and the next excited state. As one can see, the energy gap increases with the system size, instead of decreasing as one would expect, for lengths up to the excitation wavelength. Such counterintuitive behavior for the energy gap has analogously been found in photosynthetic complexes by two of the authors of this paper [37], where it has been connected to the presence of supertransfer. It is well known that such energy gaps can protect states from disorder, but the precise consequences for robustness of this gap in cylindrical aggregates need to be studied more carefully. We plan to do this in the future.

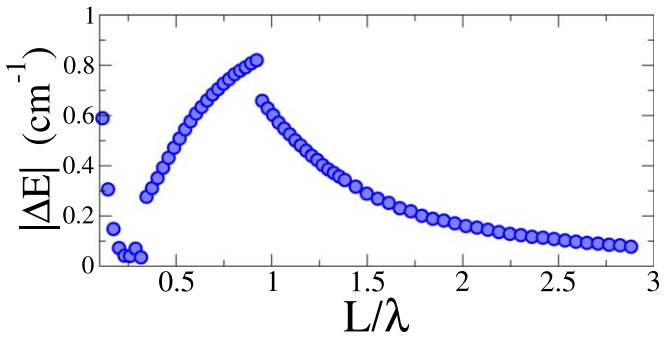

Figure C1. Energy gaps in the complex plane between the lowest exciton state and the next excited state. The gap is plotted as a function of the length of the microtubule segment normalized by the wavelength of the excitation energy of the tryptophan chromophores ($\lambda = 280$ nm).

ORCID iDs

P Kurian https://orcid.org/0000-0002-4160-6434

References

[1] Engel G S *et al* 2007 *Nature* **446** 782
[2] Panitchayangkoon G *et al* 2010 *Proc. Natl Acad. Sci. USA* **107** 12766
[3] Strumpfer J, Sener M and Schulten J 2012 *Phys. Chem. Lett.* **3** 536
[4] Lloyd S and Mohseni M 2010 *New J. Phys.* **12** 075020
[5] Celardo G L and Kaplan L 2009 *Phys. Rev.* B **79** 155108
Celardo G L *et al* 2010 *Phys. Rev.* B **82** 165437
[6] Zhang Y, Celardo G L, Borgonovi F and Kaplan L 2017 *Phys. Rev.* E **96** 052103
[7] Zhang Y, Celardo G L, Borgonovi F and Kaplan L 2017 *Phys. Rev.* E **95** 022122
[8] Giusteri G G, Celardo G L and Borgonovi F 2016 *Phys. Rev.* E **93** 032136
[9] Giusteri G G, Mattiotti F and Celardo G L 2015 *Phys. Rev.* B **91** 094301
[10] Celardo G L, Poli P, Lussardi L and Borgonovi F 2014 *Phys. Rev.* B **90** 085142
[11] Celardo G L, Giusteri G G and Borgonovi F 2014 *Phys. Rev.* B **90** 075113
[12] Celardo G L, Biella A, Kaplan L and Borgonovi F 2013 *Fortschr. Phys.* **61** 250
[13] Fetisova Z, Freiberg A and Timpmann K 1988 *Nature* **334** 633
[14] Scholes G D 2002 *Chem. Phys.* **275** 373
[15] Monshouwer R, Abrahamsson M, van Mourik V and van Grondelle R 1997 *J. Phys. Chem.* B **101** 7241
[16] Celardo G L, Borgonovi F, Tsifrinovich V I, Merkli M and Berman G P 2012 *J. Phys. Chem.* C **116** 22105
[17] Ferrari D, Celardo G L, Berman G P, Sayre R T and Borgonovi F 2014 *J. Phys. Chem.* C **118** 20
[18] Chuang C, Kong Lee C, Moix J M, Knoester J and Cao J 2016 *Phys. Rev. Lett.* **116** 196803
[19] Vlaming S M, Bloemsma E A, Linggarsari Nietiadi M and Knoester J 2011 *J. Chem. Phys.* **134** 114507
[20] Didraga C and Knoester J 2004 *J. Chem. Phys.* **121** 10687
[21] Fidder F, Knoester J and Wiersma D A 1990 *Chem. Phys. Lett.* **171** 529
[22] Spano F C and Mukamel S 1989 *J. Chem. Phys.* **91** 683
[23] Knoester J 2006 *Int. J. Photoenergy* **2006** 1–10
[24] Hu T, Damjanovic A, Ritz T and Schulten K 1998 *Proc. Natl Acad. Sci. USA* **95** 5935
[25] Craddock T J A, Friesen D, Mane J, Hameroff S and Tuszynski J A 2014 *J. R. Soc. Interface* **11** 20140677
[26] Kurian P, Obisesan T O and Craddock T J A 2017 *J. Photochem. Photobiol.* B **175** 109
[27] Kurian P, Dunston G and Lindesay J 2016 *J. Theor. Biol.* **391** 102–12
[28] Chenu A, Keren N, Paltiel Y, Nevo R and Cao J 2017 *Phys. Chem.* B **121** 9196
Eisenberg I *et al* 2014 *Phys. Chem. Chem. Phys.* **16** 11196
Eisenberg I, Caycedo-Soler F, Harris D, Yochelis S, Huelga S F, Plenio M B, Adir N, Keren N and Paltiel Y 2017 *J. Phys. Chem.* B **121** 1240
Eyal L B *et al* 2017 *Proc. Natl Acad. Sci. USA* **114** 9481
[29] Huh J *et al* 2014 *J. Am. Chem. Soc.* **136** 2048
[30] Kaznacheev A V P, Mikhailova L P and Kartashov N B 1980 *Bull. Exp. Biol. Med.* **89** 345–8
[31] Tilbury R N and Quickenden T I 1992 *J. Biolumin. Chemilumin.* **7** 245
[32] Slawinski R 2005 *Res. Complementary Med.* **12** 90–5
[33] Scholkmann F, Fels D and Cifra M 2013 *Am. J. Transl. Res.* **5** 586–93 (www.ajtr.org/files/ajtr1308004.pdf)
[34] Cifra M and Pospisil P 2014 *J. Photochem. Photobiol.* B **139** 210
[35] Albrecht-Buehler G 1994 *Cell Motil. Cytoskeleton* **27** 262–71
[36] Gross M and Haroche S 1982 *Phys. Rep.* **93** 301
[37] Gulli M, Valzelli A, Mattiotti F, Angeli M, Borgonovi F and Celardo G L 2019 *New J. Phys.* **21** 013019
[38] Yuen-Zhou J, Arias D H, Eisele D M, Steiner C P, Krich J J, Bawendi M G, Nelson K A and Aspuru-Guzik A 2014 *ACS Nano* **8** 5527
[39] Doria S *et al* 2018 *ACS Nano* **12** 4556
[40] Eisele D M *et al* 2014 *Proc. Natl Acad. Sci. USA* **111** E3367–75
[41] Eisele D M *et al* 2012 *Nat. Chem.* **4** 655

[42] Yuen-Zhou J et al 2014 ACS Nano 8 5527
[43] Caram J R et al 2016 Nano Lett. 16 6808
[44] Grad J, Hernandez G and Mukamel S 1998 Phys. Rev. A 37 3835
[45] Akkermans E, Gero A and Kaiser R 2008 Phys. Rev. Lett. 101 103602
Bienaimé T, Bachelard R, Piovella N and Kaiser R 2013 Fortschr. Phys. 61 377
[46] Weidenmulle H A 1990 Nucl. Phys. A 518 1–12
Feshbach A 1958 Ann. Phys. 5 357
Feshbach H 1962 Ann. Phys. 19 287
[47] Sokolov V V and Zelevinsky V G 1988 Phys. Lett. B 202 10
Sokolov V V and Zelevinsky V G 1989 Nucl. Phys. A 504 562
Rotter I 1991 Rep. Prog. Phys. 54 635
Izrailev F M, Sacher D and Sokolov V V 1994 Phys. Rev. E 49 130
Zelevinsky V 1996 Annu. Rev. Nucl. Part. Sci. 46 237
[48] Hu X, Ritz T, Damjanovic A and Schulten K 1997 J. Phys. Chem. B 101 3854
Hu X, Damjanovic A, Ritz T and Schulten K 1998 Proc. Natl Acad. Sci. USA 95 5935
[49] Walschaers M, Fernandez-de-Cossio Diaz J, Mulet R and Buchleitner A 2013 Phys. Rev. Lett. 111 180601
Tobias Z et al 2014 New J. Phys. 16 055002
Ortega A, Vyas M and Benet L 2015 Ann. Phys., Lpz. 527 748
Ortega A, Stegmann T and Benet L 2016 Phys. Rev. E 94 042102
[50] Anderson P W 1958 Phys. Rev. 109 1492
[51] Beenakker C W J 1997 Rev. Mod. Phys. 69 731
[52] Rodríguez A, Malyshev V A, Sierra G, Martín-Delgado M A, Rodríguez-Laguna J and Domínguez-Adame F 2003 Phys. Rev. Lett. 90 027404
Levitov L S 1989 Europhys. Lett. 9 83
[53] Albrecht-Buehler G 1977 Cell 12 333–9
[54] Albrecht-Buehler G 1992 Proc. Natl Acad. Sci. USA 89 8288–92
[55] Albrecht-Buehler G 1997 Exp. Cell Res. 236 43–50
[56] Berman H M, Westbrook J, Feng Z, Gilliland G, Bhat T N, Weissig H, Shindyalov I N and Bourne P E 2000 Nucleic Acid Res. 28 235
[57] Löwe J, Li H, Downing K H and Nogales E 2001 J. Mol. Biol. 313 1045
[58] Nogales E, Wolf S G and Downing K H 1998 Nature 39 199
[59] Li H, DeRosier D J, Nicholson W V, Nogales E and Downing K H 2002 Structure 10 1317
[60] Sept D, Baker N A and McCammon J A 2003 Protein Sci. 12 2257
[61] The PyMOL Molecular Graphics System, Version 1.8.6.2, Schrödinger LLC [http://pymol.org/]